

***Ab initio* study of the half-metal to metal transition in strained magnetite**

Martin Friák^{1,3,4}, Arno Schindlmayr^{1,2} and Matthias Scheffler¹

¹ Fritz-Haber-Institut der Max-Planck-Gesellschaft, Faradayweg 4–6, 14195 Berlin-Dahlem, Germany

² Institut für Festkörperforschung, Forschungszentrum Jülich, 52425 Jülich, Germany

E-mail: m.friak@mpie.de

New Journal of Physics **9** (2007) 5

Received 9 September 2006

Published 17 January 2007

Online at <http://www.njp.org/>

doi:10.1088/1367-2630/9/1/005

Abstract. Using density-functional theory, we investigate the stability of the half-metallic ground state of magnetite under different strain conditions. The effects of volume relaxation and internal degrees of freedom are fully taken into account. For hydrostatic compression, planar strain in the (001) plane and uniaxial strain along the [001] direction, we derive quantitative limits beyond which magnetite becomes metallic. As a major new result, we identify the bond length between the octahedrally coordinated iron atoms and their neighbouring oxygen atoms as the main characteristic parameter, and we show that the transition occurs if external strain reduces this interatomic distance from 2.06 Å in equilibrium to below a critical value of 1.99 Å. Based on this criterion, we also argue that planar strain due to epitaxial growth does not lead to a metallic state for magnetite films grown on (111)-oriented substrates.

³ Present address: Max-Planck-Institut für Eisenforschung, Max-Planck-Straße 1, 40237 Düsseldorf, Germany.

⁴ Author to whom any correspondence should be addressed.

Contents

1. Introduction	2
2. Computational method	4
3. Results	7
3.1. Hydrostatic compression	7
3.2. Tetragonal deformation in the [001] direction.	8
3.3. Rhombohedral deformation in the [111] direction	10
3.4. Internal strain	12
4. Summary	13
Acknowledgments	14
References	14

1. Introduction

Modern spintronic devices rely on the electron's spin in addition to its charge [1], but the lack of expedient materials for spintronic applications is still a major obstacle to overcome. Specific heterostructures of (semi-) conductors are required to inject, carry or manipulate spin-polarized currents. Although a variety of materials has been proposed for this purpose, only a few possess all necessary properties. Foremost is the demand of high spin polarization at ambient temperature. Excellent candidates are half-metals, first theoretically predicted by de Groot *et al* [2]. A material is termed half-metallic if electrons with only one spin orientation are present at the Fermi level. The band structure for this spin is as in metals, i.e., the Fermi level crosses partially filled bands. In contrast, electrons with the opposite spin have a band structure corresponding to an insulator, where the Fermi level falls into a band gap separating occupied from unoccupied states. In principle, an ideal 100% spin polarization of the current is thus achieved in the material.

Magnetite (Fe_3O_4) has attracted much attention as a particularly interesting spintronic material due to its high Curie temperature of 858 K. At room temperature and normal atmospheric pressure it crystallizes in a face-centred cubic spinel structure, illustrated in figure 1(a). Interestingly, this is the only crystal structure of magnetite where the positions of the atoms are known for certain. Above 25 GPa the material exhibits a high-pressure phase whose lattice is not clearly identified, but the experimental data suggest one of three possible candidates: CaMn_2O_4 , CaTi_2O_4 or CaFe_2O_4 type [3]. The low-temperature phase is even more uncertain. When cooled down, magnetite undergoes the Verwey transition [4] at about $T = 122$ K, characterized by a sharp drop in conductivity by two orders of magnitude that is accompanied by a lattice distortion with lower symmetry than the cubic spinel. The nature of the Verwey transition itself, the crystal structure as well as other characteristics of the low-temperature phase are still a topic of debate; for a comprehensive overview, we refer to recent reviews [5, 6]. The existence of these other phases has no bearing on the present study, however, which is concerned with conditions closer to ambient pressure and temperature.

In contrast to many other known half-metals, the conductivity of magnetite is not due to majority-spin but to minority-spin electrons. Recent spin-resolved photoemission experiments on the (111) surfaces of pure samples [7] demonstrated nearly ideal polarization, thus confirming previous theoretical predictions (see, e.g., [8]). For technological applications it is important that

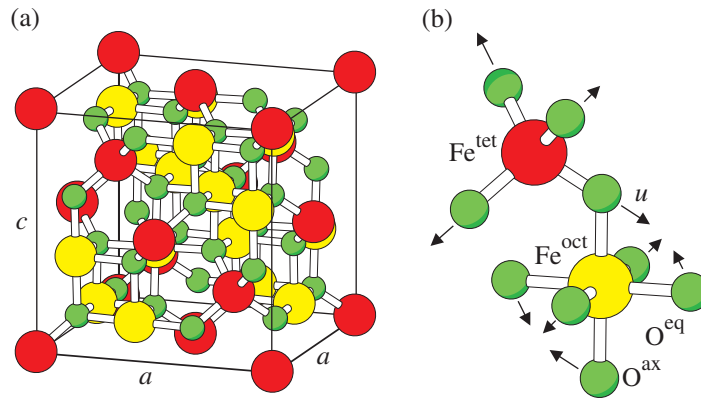


Figure 1. (a) Face-centred cubic spinel structure of magnetite. (b) Magnification of one tetrahedron and one adjacent octahedron sharing an oxygen atom. Large spheres labelled by Fe^{tet} and Fe^{oct} represent iron atoms on tetrahedrally and octahedrally coordinated sublattices, respectively. Oxygen atoms are shown as small spheres. The lattice parameters a in the (001) plane and c in the direction perpendicular to it are identical under equilibrium conditions but differ for tetragonal systems. The lower symmetry in this case also leads to the distinction between axial O^{ax} and equatorial O^{eq} atoms. Arrows indicate the shift directions of the oxygen atoms from their ideal positions for an internal parameter $u > 0$.

magnetite components in actual devices, which may incorporate magnetite elements grown on a variety of substrates with different lattice constants and orientations, behave likewise, but recent parameter-free electronic-structure calculations demonstrated that the band structures in both spin channels may become metallic if the crystal is subjected to specific kinds of strain [9]. So far the transition from the half-metallic to a metallic state was only investigated for uniaxial strain along the [001] direction with the additional constraint that the volume of the unit cell remains constant [9]. However, in systems under realistic strain conditions the volume relaxation is usually significant. In addition, for materials like magnetite with internal degrees of freedom the possible rearrangement of the atoms inside the unit cell may have a large impact on the electronic structure. The transition points extracted from such constrained calculations may hence differ substantially from the experimental phase boundaries. For this reason, we here undertake a more detailed quantitative study of the half-metal to metal transition in magnetite that also extends to a broader range of strain conditions.

Although our calculations are performed for strained bulk materials with three-dimensional (3D) periodic boundary conditions, they can be used, under certain conditions, to simulate the geometric constraints imposed by different substrates on epitaxially grown magnetite films. Due to the assumed stoichiometry and periodicity, the results may be related to experimental situations in which the prepared samples are at least 4–6 monolayers thick (depending on the substrate orientation), so that Fe_3O_4 can be distinguished from other frequently formed iron oxides with a different stoichiometric composition like FeO or Fe_2O_3 , and grown coherently, i.e., they must not be too thick to transform via relaxation processes into a bulk phase independent of the substrate or contain a large number of structural defects, such as misfit dislocations. Such films have been prepared experimentally under controlled growth conditions on a variety of substrates. For example, thin films of $\text{Fe}_3\text{O}_4(001)$ with a compressive planar strain of -0.3% were studied

on a MgO(001) substrate [10, 11], nanocrystals with a $(\bar{2}02)$ orientation and a strain of -3% were grown epitaxially on Fe(001) [12] and an even higher strain of -8% was confirmed in $\text{Fe}_3\text{O}_4(111)$ films on $\alpha\text{-Al}_2\text{O}_3(0001)$ [13]. The critical lattice misfit up to which coherent growth is possible depends on many factors, such as the substrate orientation. For example, $\text{Fe}_3\text{O}_4(001)$ films grown on $\text{SrTiO}_3(001)$, which exhibit a compressive strain of -7% , were already found to be incoherent [10]. Coherent expanded lattices, on the other hand, seem to be more easily achievable, as nanodomains of $\text{Fe}_3\text{O}_4(111)$ with an increase in the lattice constant by as much as 17% were locally observed on Ru(0001) [14].

In the following, we present an analysis of the structural, electronic and magnetic characteristics of strained magnetite with emphasis on the mechanism of the half-metal to metal transition. It takes the volume relaxation and the internal degrees of freedom into account. Only with this refined treatment can different experimental situations, such as tensile strain along the [001] direction and planar strain corresponding to epitaxial growth on a (001) substrate, which would otherwise coincide, be distinguished. As the properties of crystals may exhibit anisotropic behaviour, we consider planar strain corresponding to growth on (001)- and (111)-oriented substrates as well as uniaxial and hydrostatic strain. As a major new result of this study, we relate the occurrence of the half-metal to metal transition to threshold values of specific interatomic distances, which allows us to make predictions even for strain conditions not explicitly covered in this study.

This paper is organized as follows. In section 2, we describe our computational approach. Section 3 contains results for different strain conditions. Finally, in section 4, we summarize our conclusions.

2. Computational method

In the cubic spinel structure, illustrated in figure 1(a), the iron atoms occupy two distinct sublattices, one with tetrahedrally oxygen-coordinated and one with octahedrally oxygen-coordinated sites. These sublattices are labelled by Fe^{tet} and Fe^{oct} , respectively. The atomic basis of the minimal unit cell consists of two Fe^{tet} atoms located at $\pm(\frac{1}{8}, \frac{1}{8}, \frac{1}{8})a$ and four Fe^{oct} atoms at $(0, 0, \frac{1}{2})a$, $(\frac{1}{4}, 0, \frac{3}{4})a$, $(0, \frac{1}{4}, \frac{3}{4})a$ and $(\frac{1}{4}, \frac{3}{4}, 0)a$, where a is the lattice constant. In the ground state the oxygen atoms are shifted away from their ideal positions as shown in figure 1(b). This shift is described by an internal parameter u . A positive value implies a stretching of the $\text{Fe}^{\text{tet}}\text{-O}$ bonds and, as the oxygen atoms are shared, a trigonal distortion of the octahedra around the Fe^{oct} sites. The ultimate positions of the oxygen atoms inside the unit cell are $\pm(\frac{1}{4} + u, \frac{1}{4} + u, \frac{1}{4} + u)a$, $\pm(\frac{1}{4} + u, -u, -u)a$, $\pm(-u, \frac{1}{4} + u, -u)a$ and $\pm(-u, -u, \frac{1}{4} + u)a$. While the oxygen atoms have small magnetic moments $\mu < 0.1\mu_{\text{B}}$, where μ_{B} denotes the Bohr magneton, those of the iron atoms are more than one order of magnitude larger and antiparallel on the two sublattices. We treat all atoms belonging to the same sublattice (Fe^{tet} , Fe^{oct} or O) as equivalent, since the long-lasting dispute over the localized or itinerant character of the one extra electron per two Fe^{oct} atoms now seems to be resolved in favour of the latter, after the electronic equivalence was demonstrated both by resonant x-ray scattering [15] and self-interaction corrected *ab initio* calculations [16].

Our calculations use density-functional theory (DFT) [17] implemented within the full-potential linearized augmented-plane-wave (FP-LAPW/APW + lo) method [18]. In the explicitly spin-dependent formulation of DFT the total energy of an interacting electron system is treated as a functional of the spin densities $n_{\uparrow}(\mathbf{r})$ and $n_{\downarrow}(\mathbf{r})$ [19, 20]; the actual ground-state

spin densities minimize this functional and can thus be identified with the help of the variational principle. The Kohn–Sham scheme [21] provides a practical procedure for this variation by making the ansatz that the same spin densities can be obtained from the orbitals of an auxiliary non-interacting system as

$$n_{\sigma}(\mathbf{r}) = \sum_{\nu} \frac{V}{(2\pi)^3} \int_{\text{BZ}} f(\epsilon_{\nu\mathbf{k}\sigma}) |\varphi_{\nu\mathbf{k}\sigma}(\mathbf{r})|^2 d^3k, \quad (1)$$

where $f(\epsilon)$ is the Fermi distribution, ν denotes the band index, and the integral runs over all wave vectors \mathbf{k} inside the first Brillouin zone (BZ). The total energy is decomposed as

$$E[n_{\uparrow}, n_{\downarrow}] = T_s[n_{\uparrow}, n_{\downarrow}] + \int V_{\text{ext}}(\mathbf{r})n(\mathbf{r}) d^3r + E_H[n] + E_{\text{xc}}[n_{\uparrow}, n_{\downarrow}], \quad (2)$$

where $T_s[n_{\uparrow}, n_{\downarrow}]$ denotes the kinetic energy of the auxiliary non-interacting system, $V_{\text{ext}}(\mathbf{r})$ the crystal potential generated by the atomic nuclei in the absence of external magnetic fields and $E_H[n]$ the electrostatic Hartree energy with $n(\mathbf{r}) = n_{\uparrow}(\mathbf{r}) + n_{\downarrow}(\mathbf{r})$. Finally, $E_{\text{xc}}[n_{\uparrow}, n_{\downarrow}]$ incorporates all remaining exchange–correlation contributions. The single-particle orbitals and eigenvalues are determined from the self-consistent solution of the Kohn–Sham equations

$$\left[-\frac{1}{2}\nabla^2 + V_{\text{ext}}(\mathbf{r}) + V_H(\mathbf{r}) + V_{\sigma}^{\text{xc}}(\mathbf{r})\right] \varphi_{\nu\mathbf{k}\sigma}(\mathbf{r}) = \epsilon_{\nu\mathbf{k}\sigma} \varphi_{\nu\mathbf{k}\sigma}(\mathbf{r}), \quad (3)$$

which are derived by minimizing $E[n_{\uparrow}, n_{\downarrow}]$ with the ansatz (1) for the spin densities and the additional constraint of particle-number conservation. Here $V_H(\mathbf{r})$ denotes the Hartree potential, and the exchange–correlation potential is formally defined as the functional derivative $V_{\sigma}^{\text{xc}}(\mathbf{r}) = \delta E[n_{\uparrow}, n_{\downarrow}]/\delta n_{\sigma}(\mathbf{r})$.

Although it is well known that the Kohn–Sham eigenvalues $\epsilon_{\nu\mathbf{k}\sigma}$ do not yield the true quasi-particle band structure as measured in direct or indirect photoemission, some exact statements about the electronic properties of half-metals can still be made within this framework [22]. In particular, the eigenvalue of the highest occupied Kohn–Sham orbital in each spin channel equals the ionization potential of the bulk material and hence the corresponding quasiparticle energy. It is this property that allows a rigorous discrimination between half-metallic and metallic systems even within DFT: In the first case, the Fermi level crosses partially filled bands in the metallic spin channel but falls into a band gap separating occupied from unoccupied states in the insulating spin channel. As the valence-band maximum for this spin orientation lies below the Fermi level, the highest occupied states in the two spin channels differ. In the second case, if both spin channels are metallic, the highest occupied states are identical and equal to the Fermi level. Of course, these relations are derived for the exact exchange–correlation functional, whereas approximations must always be used in actual calculations.

To allow a full relaxation of strained systems in this study, it is essential that the exchange–correlation functional describes the ground-state volume and the interatomic distances correctly. Previous theoretical studies typically employed the local-density approximation (LDA) [23] in conjunction with different numerical schemes, such as the linear muffin-tin orbital method [8, 9] or the FP-LAPW/APW+lo method [24]. Occasionally an additional self-interaction correction was applied [16]. Performing independent structure optimizations summarized in figure 2, we find that the LDA predicts a too small equilibrium lattice constant of 8.12 Å, where magnetite is metallic with a non-integer total magnetic moment, given by the difference between occupied

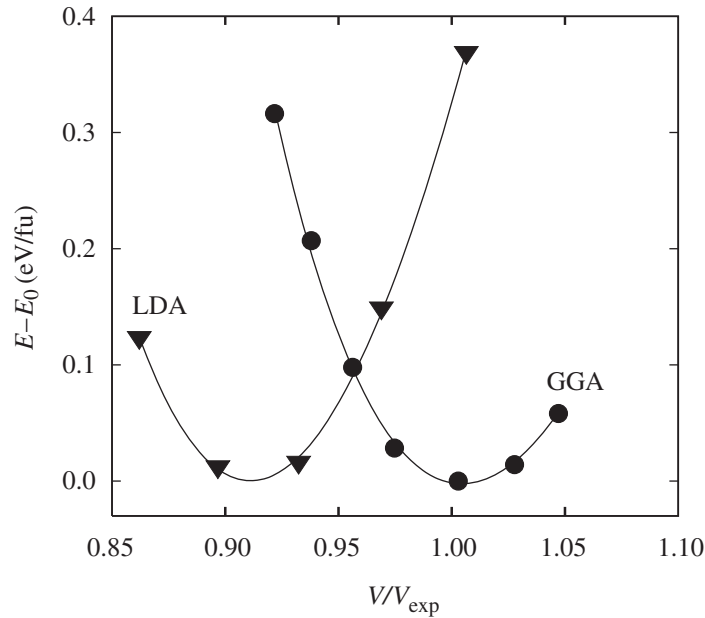


Figure 2. Total energy E of cubic magnetite relative to the equilibrium value E_0 in eV per formula unit as a function of the volume ratio V/V_{exp} , where V_{exp} is the experimental volume. The solid lines are obtained from the Murnaghan equation of state [25] with parameters fitted to the calculated results.

majority- and minority-spin states, of $3.77 \mu_B$ per formula unit (Fe_3O_4). This finding is consistent with the earlier LDA results, because the volume was not allowed to relax in these studies, and the experimental lattice parameter was used instead. Such a procedure leads to the correct half-metallic phase, but volume-constrained simulations of strained systems then preclude a full relaxation. On the other hand, we observe that the equilibrium lattice constant $a_0^{\text{th}} = 8.40 \text{ \AA}$ in the generalized gradient approximation (GGA) [26] matches the experimental value 8.39 \AA [3] almost exactly. The internal parameter 0.0051 is in equally good agreement with the experimental measurement of 0.0049 [3], as are the half-metallic behaviour and the integer magnetic moment of $4 \mu_B$. All results presented below are hence derived within the GGA.

Our calculations include relativistic effects through a solution of the fully relativistic Dirac equation for the core electrons and a scalar-relativistic treatment of the valence states [27]. For comparison, we also determined the ground-state properties without relativistic corrections for the latter and found that a structure optimization within the GGA yields very similar results in this case, a half-metallic ground state with the slightly larger equilibrium lattice constant 8.42 \AA and an unaltered value for the internal parameter. Regarding other computational details, the muffin-tin radii in this study are chosen as 1.9 bohr for iron and 1.4 bohr for oxygen. The energy cutoff E_{cut} for the interstitial plane waves equals 19.9 Ry , the maximum angular momentum l_{max} for the radial wavefunctions inside the muffin-tin spheres is set to ten and the largest reciprocal lattice vector G_{max} to 14 bohr^{-1} . When studying magnetite under different strain conditions, we use 104 , 99 and 110 k points in the irreducible part of the BZ for cubic, tetragonal and rhombohedral systems, respectively.

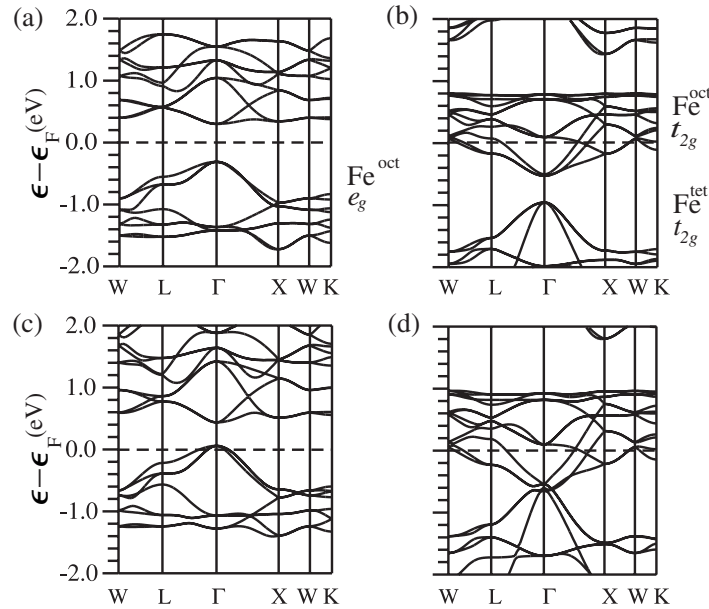


Figure 3. Majority-spin (a,c) and minority-spin (b,d) band structures of magnetite in the BZ of the face-centred cubic lattice within the GGA for the equilibrium volume (a,b) and for $V/V_0^{\text{th}} = 0.89$ (c,d). All energies are given relative to the Fermi level ϵ_F , which is marked by a dashed horizontal line.

3. Results

In figures 3(a) and (b) we illustrate the half-metallic character of the calculated Kohn–Sham band structures at the theoretical equilibrium volume V_0^{th} . The Fermi level is inside the majority-spin band gap but crosses the minority-spin bands. Its position 0.30 eV above the top of the majority-spin valence band is in excellent agreement with recent experimental measurements, which observed a threshold of 0.30 ± 0.05 eV between the onset of photoemission and the loss of the spin polarization of the electron current due to the onset of emission from the majority-spin valence bands [7]. The top of the valence band of the majority-spin electrons consists of Fe^{oct} $3d-e_g$ states ($3d_{x^2-y^2}$ and $3d_{z^2}$), hybridized with O $2p$ states, while the position of the Fermi level is determined by minority-spin Fe^{oct} $3d-t_{2g}$ states ($3d_{xy}$, $3d_{xz}$ and $3d_{yz}$). Despite the weak trigonal deformation of the octahedra, we use the e_g and t_{2g} name convention throughout this paper for simplicity.

3.1. Hydrostatic compression

Having thus confirmed that our calculations give an accurate description of the bulk equilibrium properties, we proceed to consider the influence of hydrostatic pressure. For this purpose, we vary the cubic lattice constant, performing an internal relaxation at each step. In agreement with experiment [3], we find that the internal parameter falls within a narrow interval $u \in [0.0048, 0.0053]$ without any obvious pattern as a function of volume. As the volume decreases, the energy bands broaden. As a net effect of the resulting electronic relaxation, we find that the Fermi level approaches the majority-spin valence band, eventually dropping below

the valence-band maximum at a volume reduction beyond $0.91 V_0^{\text{th}}$. The $\text{Fe}^{\text{oct}}\text{-O}$ separation, the shortest interatomic distance that determines the compression of the $3d$ states of iron, is 1.99 \AA at this point. The material thus undergoes a half-metal to metal transition as illustrated in figures 3(c) and (d). This transition is associated with topological changes of the Fermi surface, namely the creation of a recess in the centre of the BZ of the majority-spin electrons. As the majority-spin channel becomes metallic, the highest-lying valence-band states are depopulated, and electrons spin-flip into the minority-spin channel. The total magnetic moment consequently decreases from its equilibrium value of $4 \mu_{\text{B}}$ per formula unit. For the situation illustrated in figures 3(c) and (d), where the volume is compressed to $0.89 V_0^{\text{th}}$, just below the transition threshold, the magnetic moment is $3.97 \mu_{\text{B}}$ per formula unit.

It is interesting to note that the shift of the Fermi level towards the valence band of the insulating spin channel under volume reduction is opposite to theoretical predictions for another important class of half-metals, the Heusler alloys, where it approaches the conduction band [28]. This reflects the different character of the states at the band edges: in the Heusler alloys, ternary compounds with a positive spin polarization, the valence bands are formed of bonding e_g states in a cubic crystal field, while in magnetite they are formed of antibonding e_g states in a nearly-octahedral environment around the Fe^{oct} atoms.

3.2. Tetragonal deformation in the [001] direction

To investigate the mechanism of the half-metal to metal transition in a more general context and to identify the critical parameters, we now treat the spatial axes separately and study selected tetragonal deformations of magnetite in the [001] direction. Specifically, we consider two distinct scenarios, 1D uniaxial strain along the [001] direction and 2D planar strain in the (001) plane, which differ in the choice of the externally controlled lattice parameter. Due to the symmetry reduction, in tetragonal systems there are two different $\text{Fe}^{\text{oct}}\text{-O}$ interatomic bond lengths between octahedrally coordinated iron atoms and either the two nearly-axial O^{ax} or the four nearly-equatorial O^{eq} atoms as indicated in figure 1(b). Small shifts away from the ideal positions are again caused by the internal relaxation, which superimposes a trigonal deformation.

In the case of planar strain, which can serve as a simple model to simulate the deformation resulting from epitaxial growth, the in-plane lattice constant a is controlled by the substrate. In our calculation we keep it fixed at a chosen value but relax the perpendicular lattice parameter c as well as the internal parameter u . Our results, indicated by the blue line connecting the filled squares in figure 4, are in good agreement with experimental data for a magnetite film grown on a $\text{MgO}(001)$ substrate [11], marked by the empty blue square. For sufficiently large strain leading to lattice mismatches $\Delta a/a_0^{\text{th}} < -3\%$ or $\Delta a/a_0^{\text{th}} > 7\%$ a half-metal to metal transition occurs. In the contour plot the metallic states are enclosed by the yellow-shaded region. As an example, in figures 5(a) and (b) we show the band structures for $\Delta a/a_0^{\text{th}} = -3.8\%$, which are metallic in both spin channels. The reduction from cubic to tetragonal symmetry also lifts the 3-fold degeneracy of the valence-band maximum of the majority-spin electrons at Γ .

In the same manner, we simulate uniaxial strain by relaxing the parameters a and u for various values of the lattice constant c . These states are marked by the red line connecting the crosses in figure 4. We find that the half-metallic property is lost for elongations $\Delta c/a_0^{\text{th}} > 10\%$ or $\Delta c/a_0^{\text{th}} < -7\%$ in this case.

The boundary between the half-metallic and the metallic phase, indicated by the hatched line in the contour plot, is remarkably independent of c for $c/a > 1$. In fact, we find that it corresponds

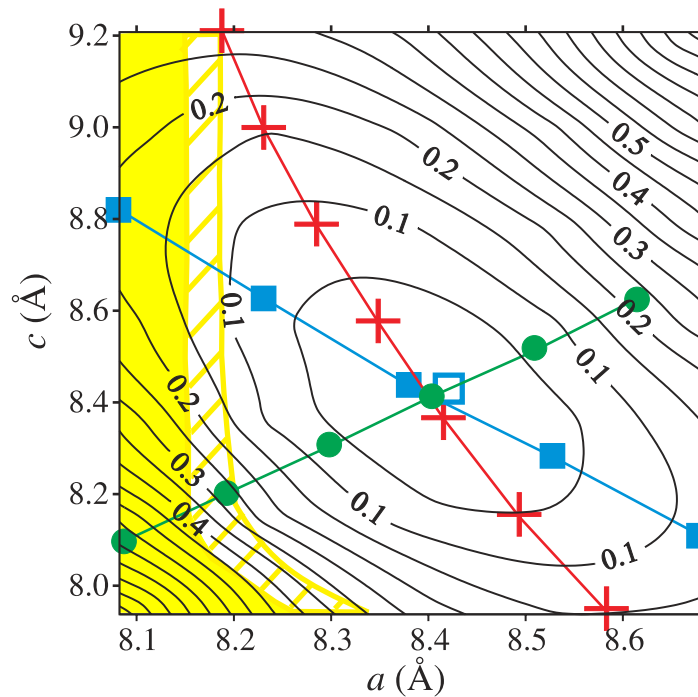


Figure 4. Contour plot of the total energy in eV per formula unit as a function of the tetragonal lattice parameters a and c . The internal parameter u is relaxed. States under isotropic pressure conditions are marked by green circles, those corresponding to epitaxial growth by blue squares, and states resulting from uniaxial compression or elongation along the [001] direction by red crosses. The empty blue square marks the experimental data for a magnetite film on a MgO(001) substrate [11]. In the yellow-shaded region our calculations predict that magnetite is metallic in both spin channels. The width of the hatched phase boundary indicates the numerical error bar.

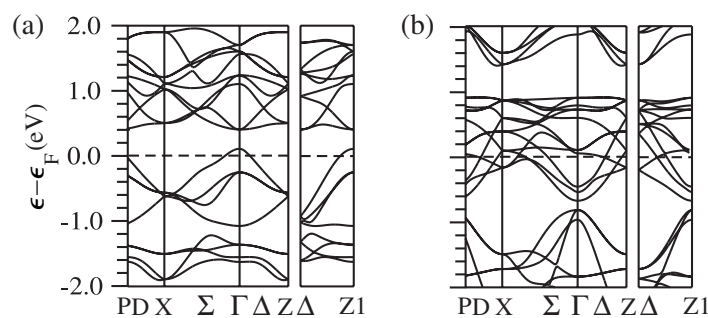


Figure 5. Majority-spin (a) and minority-spin (b) band structures of magnetite under planar compression with $\Delta a/a_0^{\text{th}} = -3.8\%$, corresponding to the left-most blue square in figure 4, in the BZ of the body-centred tetragonal lattice. Both spin channels are metallic.

to a critical distance of 1.99 Å between Fe^{oct} and the four nearly-equatorial O^{eq} atoms in the (001) plane, the same threshold value we already obtained above for isotropic volume reduction. At this point the broadening of the majority-spin Fe^{oct} $3d_{x^2-y^2}$ bands due to the in-plane compression becomes so large that they cross the Fermi level.

For tetragonal systems with $c/a < 1$ the compression along the [001] direction likewise broadens the Fe^{oct} $3d_{z^2}$ bands due to the interaction with the two nearly-axial O^{ax} atoms until they eventually intersect the Fermi level. The difference in the crystal-field environment is reflected by a slightly smaller critical distance of 1.9 Å in this case. The hatched phase boundary in figure 4 consequently changes its vertical course below the displayed region and turns into a horizontal line at $c \approx 7.6$ Å that is independent of a .

The different behaviour of magnetite under planar and uniaxial strain visible in figure 4 underlines the importance of structural relaxation. The volume changes at the transition points, in fact, range from -3% to $+6\%$ relative to V_0^{th} . Previous calculations that assumed a constant unit-cell volume [9], although giving a correct qualitative picture of the half-metal to metal transition, could not study this effect because they did not distinguish between planar and uniaxial strain. Besides, there are two further reasons for the quantitative differences between our results and those of Jeng and Guo [9], who found the transition to occur at in-plane strains of -1.3% and 2.1% , hence predicting a substantially smaller stability region for the half-metallic phase: Firstly, instead of keeping the internal parameter fixed at its equilibrium value, we take this degree of freedom explicitly into account and perform a full internal relaxation. For the states shown in figure 4, we observed values in the range $u \in [0.0040, 0.0053]$ and thus indeed a non-negligible variation of this parameter under external strain. Secondly, although the LDA that was used in [9] correctly yields a half-metallic ground state at the experimental lattice constant, it places the Fermi level much closer to the valence band of the insulating majority-spin channel than the 0.30 ± 0.05 eV found experimentally [7]. Therefore, a small deformation that would not normally induce a half-metal to metal transition can broaden the Fe^{oct} $3d-e_g$ bands enough to intersect the Fermi level in the LDA. The GGA employed here, on the other hand, does not suffer from this problem, because it yields the correct position of the Fermi level relative to the top of the majority-spin valence band.

3.3. Rhombohedral deformation in the [111] direction

As another lattice deformation that may be relevant for the design of technological applications involving magnetite, we now study uniaxial strain along the [111] direction and planar strain in the (111) plane. The latter may serve as a model to simulate the effect of growth on a (111)-oriented substrate. In either case, the deformation leads to crystals with a rhombohedral unit cell that are most conveniently described by the hexagonal lattice parameters. These take the values $a_0^{\text{hex}} = a_0^{\text{th}}/\sqrt{2}$ and $c_0^{\text{hex}} = \sqrt{3}a_0^{\text{th}}$ in the absence of strain, where a_0^{th} denotes the cubic lattice constant. As a consequence of the symmetry reduction, atoms that were crystallographically equivalent in the unstrained cubic phase now start to form distinct inequivalent sublattices, so that the systems under investigation exhibit a large number of internal degrees of freedom. Unfortunately, this structural complexity prevented us from performing a full internal relaxation, as we did for tetragonal deformations. As shown above, however, in that case the internal parameter only fluctuated within a limited interval and exhibited no systematic trend. Assuming a similar situation here, we hence kept the atoms at the same relative positions inside the unit cell as in the unstrained cubic ground state. In this way, we performed calculations for uniaxial

strain along the [111] direction with $\Delta c^{\text{hex}}/c_0^{\text{hex}}$ spanning the interval from -5.5% to $+9\%$, and we investigated planar (111) strain with $\Delta a^{\text{hex}}/a_0^{\text{hex}}$ in the range from -3.5% to $+3.5\%$, the lower limit in each case being dictated by the constraint of non-overlapping muffin-tin spheres.

Unlike the situation of tetragonal states considered in the previous section, we found no transition to a metallic phase for uniaxial [111] or planar (111) strain. Its absence, in fact, is not surprising and can be understood by a simple geometric argument. As we already argued above, the half-metal to metal transition in magnetite is caused by the broadening of the $\text{Fe}^{\text{oct}} 3d-e_g$ states that form the valence band of the insulating majority-spin channel. This broadening, in turn, results from the compression of the $\text{Fe}^{\text{oct}}\text{-O}$ bonds, and the transition sets in if this interatomic distance falls below a critical value. For tetragonal states this must always occur eventually, because the strain is parallel to the direction of the bonds, but for rhombohedral deformations the situation is very different. If we neglect the internal degree of freedom by setting $u = 0$, then the oxygen atoms around Fe^{oct} initially form a perfect octahedron with vertices located equidistant along the Cartesian axes. If we further ignore volume relaxation for the moment, then the rhombohedral deformation can be described by a single parameter $\lambda = a^{\text{hex}}/a_0^{\text{hex}} = (c^{\text{hex}}/c_0^{\text{hex}})^{-1/2}$, with $\lambda = 1$ in the absence of strain. A simple geometric consideration shows that strain along the [111] direction enhances the $\text{Fe}^{\text{oct}}\text{-O}$ distance by a factor

$$\sqrt{\left(\frac{1}{3\lambda^2} + \frac{2\lambda}{3}\right)^2 + 2\left(\frac{1}{3\lambda^2} - \frac{\lambda}{3}\right)^2} = 1 + 2(\lambda - 1)^2 + O((\lambda - 1)^3) \quad (4)$$

in this scenario, i.e., it is increased both by compression and elongation along the [111] direction and thus never falls below its critical value. Neither volume relaxation nor the displacement of the oxygen atoms due to a non-zero internal parameter u change this conclusion qualitatively.

Under these circumstances a half-metal to metal transition can, in fact, only be forced if both hexagonal lattice parameters are independently reduced to rather extreme values. Nevertheless, it is illuminating to explore the phase boundary by varying a_0^{hex} and c_0^{hex} systematically. In this way, we find once more that the transition occurs precisely if the $\text{Fe}^{\text{oct}}\text{-O}$ distance falls below the critical value of 1.99 \AA . As rhombohedral deformations involve a combination of uniaxial [001] and planar (001) strain, this threshold is reached before the lower value of 1.9 \AA that we identified for the nearly-axial oxygen atoms and is therefore applicable. Such extreme states can only be reached if significant compressive strain is applied simultaneously along the [111] direction and in the (111) plane, however.

As an example for a metallic state induced by rhombohedral deformation, we show the band structures of magnetite with lattice parameters $\Delta a^{\text{hex}}/a_0^{\text{hex}} = -5.5\%$ and $\Delta c^{\text{hex}}/c_0^{\text{hex}} = -3.5\%$ in figures 6(c) and (d). The $\text{Fe}^{\text{oct}}\text{-O}$ interatomic distance is 1.97 \AA in this case. For comparison, the band structures of unstrained cubic magnetite are redrawn in figures 6(a) and (b) along the same high-symmetry lines of the hexagonal lattice. The effect of the strain on the band structure is similar to that of other compressive deformations investigated above. The Fermi level gradually approaches the valence band of the majority-spin electrons. As for tetragonal states, the symmetry reduction also lifts the 3-fold degeneracy of the valence-band maximum of the majority-spin electrons at Γ in the case of rhombohedral deformation.

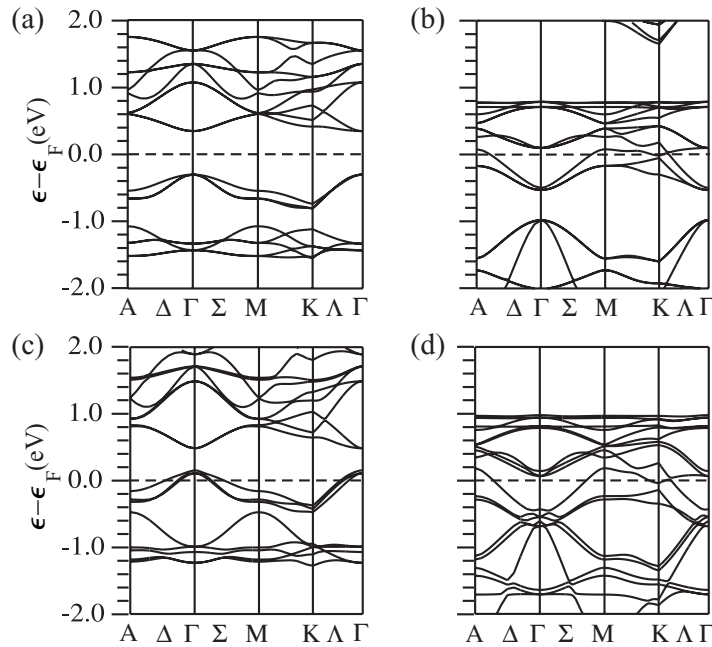


Figure 6. Majority-spin (a,c) and minority-spin (b,d) band structures in the BZ of the hexagonal lattice for unstrained magnetite (a,b) and for a rhombohedral deformation with $\Delta a^{\text{hex}}/a_0^{\text{hex}} = -5.5\%$ and $\Delta c^{\text{hex}}/c_0^{\text{hex}} = -3.5\%$ that leads to a metallic phase.

3.4. Internal strain

The results obtained in the previous sections provide strong evidence that the half-metal to metal transition in magnetite is controlled by a single geometric parameter, the $\text{Fe}^{\text{oct}}\text{-O}$ interatomic distance. In order to test this hypothesis, we now focus exclusively on the internal degrees of freedom. Specifically, we keep the cubic lattice parameters at their equilibrium values $a = c = 8.40 \text{ \AA}$ and merely shift the oxygen atoms inside the unit cell by increasing the internal parameter u . This displacement of the oxygen atoms, illustrated in figure 1(b), corresponds to an expansion of the tetrahedra around Fe^{tet} and a trigonal distortion of the octahedra around Fe^{oct} . As the oxygen atoms approach the latter simultaneously along the [001] direction and in the (001) plane, we again expect the larger of the two values for the critical interatomic distance to be decisive here. Indeed, we find that the half-metal to metal transition occurs precisely at $u = 0.0135$, where the $\text{Fe}^{\text{oct}}\text{-O}$ distance equals 1.99 \AA . The band structures at this point are displayed in figures 7(a) and (b) and should be compared to the equilibrium band structures in figures 3(a) and (b).

Interestingly, the strong influence of the internal degrees of freedom on the electronic structure also suggests a possible coupling between vibrational modes and the electronic properties of magnetite. We will explore this connection in a future study.

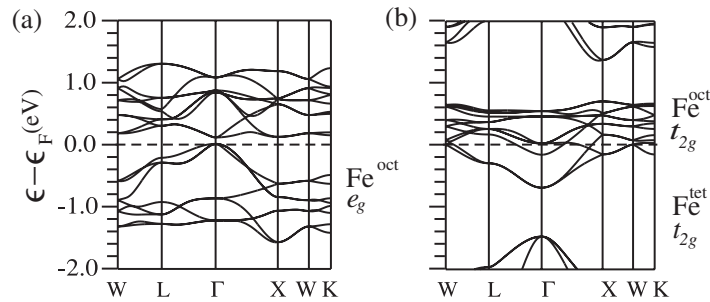


Figure 7. Majority-spin (a) and minority-spin (b) band structures of magnetite in the BZ of the face-centred cubic lattice at the equilibrium volume but with a displacement of the oxygen atoms inside the unit cell corresponding to the internal parameter $u = 0.0135$, where the $\text{Fe}^{\text{oct}}\text{-O}$ interatomic distance falls below the critical value 1.99 \AA for the half-metal to metal transition.

4. Summary

We have provided an analysis of the electronic structure of strained magnetite with special focus on the mechanism of the half-metal to metal transition. In all cases where a strain-induced transition occurs, we found that it is characterized by a shift of the Fermi level below the valence-band maximum of the majority-spin channel, which consists of $\text{Fe}^{\text{oct}} 3d\text{-}e_g$ states. By investigating a wide range of different strain conditions, we explained this behaviour and showed that it is, in fact, controlled by a single parameter, the $\text{Fe}^{\text{oct}}\text{-O}$ interatomic distance: a compression of the bonds between the central iron atom and the oxygen atoms at the vertices of its nearly-octahedral environment broadens the valence band until it intersects the Fermi level, thus leading to a metallic phase. As a major new result of this study, we obtained a quantitative criterion by demonstrating that the transition occurs if the $\text{Fe}^{\text{oct}}\text{-O}$ interatomic distance falls from 2.06 \AA in equilibrium to below a critical value of 1.99 \AA . The only significant deviation was observed for a compression purely parallel to the $[001]$ axis, where we found a value of 1.9 \AA instead, but as external strain typically leads to deformations of the unit cell in multiple directions, the higher threshold of 1.99 \AA is usually reached first and therefore applicable in general situations.

Based on all-electron DFT calculations, we showed explicitly that the half-metal to metal transition in magnetite may be induced by (i) hydrostatic compression, i.e., isotropic volume reduction, below $0.91V_0^{\text{th}}$, (ii) planar strain in the (001) plane due to lattice mismatches $\Delta a/a_0^{\text{th}} < -3\%$ or $\Delta a/a_0^{\text{th}} > 7\%$ and (iii) uniaxial strain along the $[001]$ direction with $\Delta c/a_0^{\text{th}} < -7\%$ or $\Delta c/a_0^{\text{th}} > 10\%$. These phase boundaries differ from the values reported in [9], because here we take the volume relaxation upon planar or uniaxial strain as well as the internal degrees of freedom fully into account. In addition, use of the GGA instead of the LDA exchange–correlation functional in this study eliminates systematic errors by ensuring the proper position of the valence band relative to the Fermi level in equilibrium. Finally, employing our geometric criterion, we explained why planar strain due to epitaxial growth on a substrate with different lattice constant can induce a half-metal to metal transition for magnetite films oriented along $[001]$, if the lattice mismatch exceeds the above boundaries, but not for $[111]$ -oriented films. In this case, the rhombohedral deformation of the unit cell always increases the $\text{Fe}^{\text{oct}}\text{-O}$ interatomic distance, so that it never falls below the critical value.

Acknowledgments

This study was funded in part by the EU through the Nanophase Research Training Network (HPRN-CT-2000-00167) and the Nanoquanta Network of Excellence (NMP4-CT-2004-500198).

References

- [1] Chambers S A and Yoo Y K 2003 New materials for spintronics *MRS Bull.* **28** 706–7
- [2] de Groot R A, Mueller F M, van Engen P G and Buschow K H J 1983 New class of materials: half-metallic ferromagnets *Phys. Rev. Lett.* **50** 2024–7
- [3] Haavik C, Stölen S, Fjellvåg H, Hanfland M and Häusermann D 2000 Equation of state of magnetite and its high-pressure modification: thermodynamics of the Fe–O system at high pressure *Am. Mineral.* **85** 514–23
- [4] Verwey E J W 1939 Electronic conduction of magnetite (Fe₃O₄) and its transition point at low temperature *Nature* **144** 327–8
- [5] Walz F 2002 The Verwey transition—a topical review *J. Phys.: Condens. Matter* **14** R285–340
- [6] García J and Subías G 2004 The Verwey transition—a new perspective *J. Phys.: Condens. Matter* **16** R145–78
- [7] Dedkov Y S, Rüdiger U and Güntherodt G 2002 Evidence for the half-metallic ferromagnetic state of Fe₃O₄ by spin-resolved photoelectron spectroscopy *Phys. Rev. B* **65** 064417-1–5
- [8] Zhang Z and Satpathy S 1991 Electronic states, magnetism, and the Verwey transition in magnetite *Phys. Rev. B* **44** 13319–31
- [9] Jeng H-T and Guo G Y 2002 First-principles investigations of the electronic structure and magnetocrystalline anisotropy in strained magnetite Fe₃O₄ *Phys. Rev. B* **65** 094429-1–9
- [10] Li X W, Gupta A, Xiao G and Gong G Q 1998 Transport and magnetic properties of epitaxial and polycrystalline magnetite thin films *J. Appl. Phys.* **83** 7049–51
- [11] Kale S *et al* 2001 Film thickness and temperature dependence of the magnetic properties of pulsed-laser-deposited Fe₃O₄ films on different substrates *Phys. Rev. B* **64** 205413-1–9
- [12] Yi W, MoberlyChan W, Narayanamurti V, Hu Y F, Li Q, Kaya I, Burns M and Chen D M 2004 Characterization of spinel iron-oxide nanocrystals grown on Fe whiskers *J. Appl. Phys.* **95** 7136–8
- [13] Gota S, Moussy J-B, Henriot M, Guittet M-J and Gautier-Soyer M 2001 Atomic-oxygen-assisted MBE growth of Fe₃O₄(111) on α -Al₂O₃(0001) *Surf. Sci.* **482–5** 809–16
- [14] Ketteler G and Ranke W 2003 Heteroepitaxial growth and nucleation of iron oxide films on Ru(0001) *J. Phys. Chem. B* **107** 4320–33
- [15] García J, Subías G, Proietti M G, Renevier H, Joly Y, Hodeau J L, Blasco J, Sánchez M C and Bézar J F 2000 Resonant ‘forbidden’ reflections in magnetite *Phys. Rev. Lett.* **85** 578–81
- [16] Szotek Z, Temmerman W M, Svane A, Petit L, Stocks G M and Winter H 2003 *Ab initio* study of charge order in Fe₃O₄ *Phys. Rev. B* **68** 054415-1–9
- [17] Hohenberg P and Kohn W 1964 Inhomogeneous electron gas *Phys. Rev.* **136** B864–71
- [18] Blaha P, Schwarz K, Madsen G K H, Kvasnicka D and Luitz J 2001 *WIEN2k: an augmented plane wave plus local orbitals program for calculating crystal properties* (Vienna: Technische Universität Wien)
- [19] von Barth U and Hedin L 1972 A local exchange-correlation potential for the spin polarized case *J. Phys. C: Solid State Phys.* **5** 1629–42
- [20] Gunnarsson O and Lundqvist B I 1976 Exchange and correlation in atoms, molecules, and solids by the spin-density-functional formalism *Phys. Rev. B* **13** 4274–98
- [21] Kohn W and Sham L J 1965 Self-consistent equations including exchange and correlation effects *Phys. Rev.* **140** A1133–38
- [22] Eschrig H and Pickett W E 2001 Density functional theory of magnetic systems revisited *Solid State Commun.* **118** 123–7
- [23] Perdew J P and Wang Y 1992 Accurate and simple analytic representation of the electron-gas correlation energy *Phys. Rev. B* **45** 13244–9

- [24] Yanase A and Hamada N 1999 Electronic structure in high temperature phase of Fe_3O_4 *J. Phys. Soc. Japan* **64** 1607–13
- [25] Murnaghan F D 1944 The compressibility of media under extreme pressures *Proc. Natl Acad. Sci. USA* **30** 244–7
- [26] Perdew J P, Burke K and Ernzerhof M 1996 Generalized gradient approximation made simple *Phys. Rev. Lett.* **77** 3865–8
- [27] Koelling D D and Harmon B N 1977 A technique for relativistic spin-polarised calculations *J. Phys. C: Solid State Phys.* **10** 3107–14
- [28] Picozzi S, Continenza A and Freeman A J 2002 Co_2MnX ($X = \text{Si}, \text{Ge}, \text{Sn}$) Heusler compounds: an *ab initio* study of their structural, electronic, and magnetic properties at zero and elevated pressure *Phys. Rev. B* **66** 094421